## Interstellar Comet 3I/ATLAS: Evidence for Galactic Cosmic Ray Processing

ROMAIN MAGGIOLO, <sup>1</sup> FREDERIK DHOOGHE, <sup>1</sup> GUILLAUME P. GRONOFF, <sup>2,3</sup> JOHAN DE KEYSER, <sup>1,4</sup> AND GAËL CESSATEUR <sup>1</sup>

<sup>1</sup>Royal Belgian Institute for Space Aeronomy (BIRA-IASB) Brussels, Belgium
<sup>2</sup>Science Systems and Application Inc. Hampton, Va, USA
<sup>3</sup>Nasa Langley Research Center, Hampton, Va, USA
<sup>4</sup>Centre for mathematical Plasma Astrophysics, Heverlee, Belgium

## ABSTRACT

Spectral observations of 3I/ATLAS (C/2025 N1) with JWST/NIRSpec and SPHEREx reveal an extreme  $CO_2$  enrichment ( $CO_2/H_2O = 7.6\pm0.3$ ) that is 4.5  $\sigma$  above solar system comet trends and among the highest ever recorded. This unprecedented composition, combined with substantial absolute CO levels ( $CO/H_2O = 1.65\pm0.09$ ) and red spectral slopes, provides direct evidence for galactic cosmic ray (GCR) processing of the outer layers of the interstellar comet nucleus.

Laboratory experiments demonstrate that GCR irradiation efficiently converts CO to  $\rm CO_2$  while synthesizing organic-rich crusts, suggesting that the outer layers of 3I/ATLAS consist of irradiated material which properties are consistent with the observed composition of 3I/ATLAS coma and with its observed spectral reddening. Estimates of the erosion rate of 3I/ATLAS indicate that current outgassing samples the GCR-processed zone only (depth  $\sim 15-20$  m), never reaching pristine interior material. Outgassing of pristine material after perihelion remains possible, though it is considered unlikely.

This represents a paradigm shift: long-residence interstellar objects primarily reveal GCR-processed material rather than pristine material representative of their primordial formation environments. With 3I/ATLAS approaching perihelion in October 2025, immediate follow-up observations are critical to confirm this interpretation and establish GCR processing as a fundamental evolutionary pathway for interstellar objects.

Keywords: Comets (280) Interstellar objects (52) Comet nuclei (2160) Cosmic rays (329) Galactic cosmic rays (567)

## 1. INTRODUCTION

The discovery of interstellar objects 1I/'Oumuamua and 2I/Borisov has opened a new window into the composition and evolution of small bodies from other stellar systems. 1I/'Oumuamua exhibited puzzling non-gravitational acceleration despite showing no detectable outgassing, suggesting either exotic composition or unusual surface properties (Micheli et al. 2018; Seligman & Laughlin 2020). 2I/Borisov displayed more conventional cometary activity but with unusually high CO enrichment relative to solar system comets, indicating potential differences in formation environment or evolutionary history (Bodewits et al. 2020; Cordiner et al. 2020).

A fundamental question for understanding interstellar objects concerns how extended residence in the galactic environment affects their composition and surface properties. Dose deposition models for solar system comets over Gyr timescales (Gronoff et al. 2020), combined with laboratory experiments on cometary ice analogs (Johnson & Quickenden 1997; Hudson & Moore 1999; Dartois et al. 2015), show that galactic cosmic ray (GCR) irradiation can substantially alter nucleus material over Gyr time scales, modifying its original chemical composition and ice structure (Maggiolo et al. 2020). However, no direct observational evidence for such processing has been identified in confirmed interstellar visitors.

Email: romain.maggiolo@aeronomie.be

The interstellar comet 3I/ATLAS (C/2025 N1) was discovered on 2025 July 1 by the Asteroid Terrestrial-impact Last Alert System (ATLAS; Tonry et al. 2018) from Rio Hurtado, Chile. Its interstellar nature was confirmed the following day (Denneau et al. 2025). This third interstellar object provides a new opportunity to investigate these questions. The object follows a strongly hyperbolic trajectory ( $e \simeq 6.1, q \simeq 1.36$  AU,  $i \simeq 175^{\circ}, V_{\infty} \simeq 58$  km s<sup>-1</sup>), confirming its extrasolar origin (Seligman et al. 2025; Bolin et al. 2025). High-resolution imaging constrains the effective nucleus radius to  $r \lesssim 2.8$  km, with volatile-dependent lower bounds of  $r \gtrsim 0.22$ –1.1 km derived from coma properties (Jewitt et al. 2025).

Dynamical analyses of 3I/ATLAS suggest it is the oldest known interstellar object, with kinematic models estimating its age between 3 and 11 Gyr (Taylor & Seligman 2025). galactic orbit comparisons indicate it likely originated from an ancient, metal-poor stellar population older than 7.6 Gyr (Hopkins et al. 2025). Early spectroscopic observations reveal active outgassing with compositional signatures that differ markedly from both previous interstellar objects and solar system comets.

In this communication, we discuss spectroscopic observations of 3I/ATLAS within the framework of cosmic ray processing mechanisms. We demonstrate that the observed signatures provide compelling evidence for Gyr-scale galactic cosmic ray alteration of the outer layers of 3I/ATLAS's nucleus, with implications for interpreting the composition of ancient visitors from other stellar systems.

## 2. OBSERVATIONS

# 2.1. Spectroscopic Measurements

Near-nucleus JWST/NIRSpec Integral Field Unit (IFU) spectra obtained on UT 2025 August 6 at a heliocentric distance of  $r_{\rm h} \simeq 3.32$  au reveal a coma dominated by CO<sub>2</sub> outgassing with detectable CO and H<sub>2</sub>O production close to the nucleus. From the nucleus-centered extract, Cordiner et al. (2025) derive production rates of  $Q(CO_2) = (9.50 \pm 0.08) \times 10^{26} \ {\rm s}^{-1}$ ,  $Q(CO) = (1.70 \pm 0.04) \times 10^{26} \ {\rm s}^{-1}$ , and  $Q(H_2O) = (1.07 \pm 0.07) \times 10^{26} \ {\rm s}^{-1}$ . Based on their Q-curve analysis, Cordiner et al. (2025) estimate the total coma-equivalent gas production rates for 3I/ATLAS. The Q-curves show CO<sub>2</sub> and CO flatten by  $\sim 3000$  km, indicating that gas production for these species is confined within  $\sim 3000$  km of the nucleus. The H<sub>2</sub>O Q-curve shows no clear asymptote, providing evidence for an extended water source.

The resulting terminal gas production rates are  $Q(\text{CO}_2) = (1.70 \pm 0.01) \times 10^{27} \text{ s}^{-1}$ ,  $Q(\text{CO}) = (3.7 \pm 0.2) \times 10^{26} \text{ s}^{-1}$ ,  $Q(\text{H}_2\text{O}) = (2.23 \pm 0.08) \times 10^{26} \text{ s}^{-1}$ , and  $Q(\text{OCS}) = (1.7 \pm 0.9) \times 10^{24} \text{ s}^{-1}$ . Based on the Q-curve terminal values, the coma-averaged mixing ratios are  $\text{CO}_2/\text{H}_2\text{O} = 7.6 \pm 0.3$  and  $\text{CO}/\text{H}_2\text{O} = 1.65 \pm 0.09$ .

Complementary SPHEREx measurements (2025 August 12,  $r_{\rm h} \simeq 3.1$ –3.3 au) find  $Q({\rm CO_2}) \approx 9.4 \times 10^{26}~{\rm s^{-1}}$ , and  $3\sigma$  upper limits of  $Q({\rm H_2O}) \leq 1.5 \times 10^{26}~{\rm s^{-1}}$  and  $Q({\rm CO}) \leq 2.8 \times 10^{26}~{\rm s^{-1}}$ . These are qualitatively consistent with JWST's CO<sub>2</sub> dominance and weaker  ${\rm H_2O/CO}$  near the nucleus. Quantitatively, JWST's terminal  ${\rm H_2O}$  production rate  $(2.19 \times 10^{26}~{\rm s^{-1}})$  is modestly above the SPHEREx  $3\sigma$  limit, which is reasonable given the different apertures and sensitivities (Lisse et al. 2025).

Swift/UVOT OH imaging yields  $Q(\mathrm{H_2O}) = (0.74 \pm 0.50) \times 10^{27} \mathrm{\ s^{-1}}$  at  $r_{\mathrm{h}} = 3.51 \mathrm{\ au}$  (2025 July 31) and (1.36  $\pm$  0.35)  $\times$  10<sup>27</sup> s<sup>-1</sup> at  $r_{\mathrm{h}} = 2.90 \mathrm{\ au}$  (2025 August 19), measured in a 10"-radius ( $\simeq 2.0 \times 10^4 \mathrm{\ km}$ ) aperture (Xing et al. 2025). The larger-aperture Swift rates, together with JWST's outward-increasing H<sub>2</sub>O Q-curve, support an extended water source.

The color and spectral properties of 3I/ATLAS have been characterized through photometric and spectroscopic observations spanning the visible to near-infrared. 3I/ATLAS consistently exhibits a steep, red spectral slope and color indices indicative of a red continuum. Spectrophotometry yields color indices of  $g-r\simeq 0.60$  and  $r-i\simeq 0.21$ , consistent with its red reflectance spectrum (Beniyama 2025). Photometry yields color indices such as  $B-V=0.98\pm 0.23$ ,  $V-R=0.71\pm 0.09$ , and  $g-r=0.84\pm 0.05$ , corresponding to a reflectance slope of  $(16.0\pm 1.9)\%/100$  nm (Bolin et al. 2025). Spectrophotometric measurements corroborate these findings, reporting slopes of  $\sim 19\%/100$  nm over 420–700 nm (Belyakov et al. 2025), 18.3  $\pm 0.9\%/100$  nm across 400–900 nm (Marcos de la Fuente et al. 2025), and 17.1  $\pm 0.2\%/100$  nm across 420–700 nm (Seligman et al. 2025). In the near-infrared, the slope flattens, trending toward neutral or slightly blue reflectance beyond  $\sim 1.1~\mu$ m (Belyakov et al. 2025; Kareta et al. 2025). Despite broad agreement on its red spectral character, precise interpretation is hindered by coma dominance, instrumental systematics, and poorly constrained dust properties (e.g., Seligman et al. 2025; Kareta et al. 2025).

## 2.2. Comparison with Known Populations

The  $CO_2/H_2O$  ratio of  $7.6 \pm 0.3$  places 3I/ATLAS among the most  $CO_2$ -enriched objects observed. Compared to solar system comets, the comprehensive survey of Harrington-Pinto et al. (2022) reported a median  $CO_2/H_2O$  ratio of  $0.12\pm0.02$  across 25 comets, with a few outliers reaching up to, but not exceeding,  $\sim$ 0.3 in individual cases (Harrington-Pinto et al. 2022), consistent with the upper values reported in earlier surveys (Ootsubo et al. 2012; McKay et al. 2015). The statistical significance places the  $CO_2/H_2O$  ratio  $4.5\sigma$  above solar system trends (Cordiner et al. 2025), although this enrichment must be interpreted cautiously given observational selection effects and the limited sample of comets observed at comparable heliocentric distances where  $CO_2$  can be measured. This ratio also significantly exceeds interstellar medium  $CO_2/H_2O$  ice abundances, typically  $\sim$ 10–30% with environment-dependent maxima up to  $\sim$ 40–50%, as summarized by Boogert et al. (2015) and confirmed in JWST background-star sightlines ( $\sim$ 10–20%) by McClure et al. (2023).

The high CO/H<sub>2</sub>O ratio (1.65  $\pm$  0.09) also greatly exceeds the solar system median of 0.03  $\pm$  0.01 (Harrington-Pinto et al. 2022). Most comets inside  $\sim$ 3 au span 0.002–0.23 (Bockelée-Morvan & Biver 2017). This enrichment is similar to 2I/Borisov, which showed CO/H<sub>2</sub>O  $\approx$  1.3–1.55 near perihelion (Bodewits et al. 2020), suggesting possible commonalities among interstellar objects that may reflect shared formation or evolutionary processes.

The spectral slope of 3I/ATLAS places it among the reddest small bodies known in the solar system. Its visible continuum is considerably steeper than that observed in typical cometary comae (Opitom et al. 2025), yet is comparable to the slopes measured for interstellar objects such as 1I/'Oumuamua (Fitzsimmons et al. 2018) and 2I/Borisov (de León et al. 2020). Within solar system reservoirs, 3I/ATLAS overlaps with the redder members of the Centaur population (Fornasier et al. 2009), including very red objects such as Pholus, and is consistent with the spectrophotometry of trans-Neptunian objects (TNOs) such as 2012 DR30, whose reflectance spectrum exhibits a pronounced reddening in the near-UV (Seccull et al. 2021). 3I/ATLAS is less red than the "ultrared" cold classical TNOs, which display the steepest optical slopes among trans-Neptunian populations, as shown by the HST/WFC3 survey (Fraser & Brown 2012) and more recent JWST observations (Souza-Feliciano, A. C. et al. 2024). Many of these objects also exhibit deviations from a strictly linear reddening trend in the near-infrared (Seccull et al. 2021). Its slope also falls within the range of D-type asteroids, known for their steep, red, featureless spectra (Fitzsimmons et al. 1994).

# 3. EVIDENCE FOR COSMIC RAY PROCESSING IF 3I/ATLAS

# 3.1. Primordial and Post-Formation Pathways for 3I/ATLAS's Observed Properties

JWST/NIRSpec measurements show  $CO_2/H_2O = 7.6 \pm 0.3$ , placing 3I/ATLAS 4.5 $\sigma$  above solar system trends at the observed heliocentric distance. Any viable explanation must therefore elevate the near-surface  $CO_2/H_2O$  ratio substantially.

Multiple processes could contribute to the unusual volatile inventory of comets. Physical conditions during the formation of protoplanetary discs (e.g., Drozdovskaya et al. 2016) and chemical evolution within protoplanetary disks can alter CO and CO<sub>2</sub> abundances depending on disk conditions (e.g., Eistrup et al. 2018). In addition, non-thermal processing of ices by GCR and UV photons in dense molecular clouds and protoplanetary disks can modify ice composition before incorporation into planetesimals, thereby influencing the volatile make-up inherited by comets (Semenov et al. 2004). Pebble drift mechanisms can yield  $CO/H_2O \gtrsim 10$  by creating CO-rich rings (Price et al. 2021), but because CO<sub>2</sub> condenses closer to the star than CO, their snowlines are spatially separated, preventing simultaneous enhancement of both species in the same reservoir. Additional disk pathways, such as midplane CO destruction that converts CO into CO<sub>2</sub> and other species (Bosman et al. 2018), or clathrate trapping and amorphous-ice inheritance affecting volatile budgets (Mousis et al. 2010), can alter carbon-oxygen partitioning but likewise struggle to reproduce simultaneously CO<sub>2</sub>- and CO-rich ices at the observed level. Statistical comparisons of disk chemical evolution models with cometary observations confirm partial agreement but reveal persistent mismatches in CO/CO<sub>2</sub> ratios, even when formation is assumed near the CO snowline (Eistrup et al. 2019). Taken together, these primordial scenarios each reproduce certain aspects of cometary volatile inventories but struggle to account for the simultaneous presence of both CO- and CO<sub>2</sub>-rich ices. This motivates consideration of post-formation processes that could further modify initial compositions. GCR processing merits particular attention given indications that 3I/ATLAS may be an ancient interstellar object and the well-documented effects of energetic particle irradiation on ice composition.

Experimental results consistently demonstrate that irradiation of H<sub>2</sub>O–CO and H<sub>2</sub>O–CO<sub>2</sub> ices by energetic particles leads to CO<sub>2</sub> formation. This process was identified in ion-irradiation studies (Palumbo 1997) and was subsequently confirmed through proton bombardment of mixed ices (Hudson & Moore 1999). These findings have been extended

across a broad range of ice compositions, temperatures, and radiation sources, including both ions and ultraviolet photons (Gerakines et al. 2001). Cold H<sub>2</sub>O-CO ices, analogous to those found in dense molecular clouds and cometary environments, reliably show efficient CO<sub>2</sub> synthesis, with yields modulated by ice thickness, mixing ratio, projectile energy, and temperature (Gerakines et al. 2001; Mennella et al. 2004). Furthermore, CO<sub>2</sub> formation occurs readily from various C-O-bearing ice mixtures (e.g., Palumbo 1997; Baratta et al. 2002). Despite the consistent production of CO<sub>2</sub>, CO is not entirely consumed; multiple studies report that CO persists in the irradiated ice (e.g., Palumbo 1997; Satorre et al. 2000; Mennella et al. 2004). Notably, ion-irradiation experiments involving CO<sub>2</sub>, either as pure ice or in mixtures, show that the  $CO_2/CO$  ratio stabilizes at approximately 0.1 after a fluence of  $\sim 2-3 \times 10^{12}$  ions cm<sup>-2</sup>, independent of the initial CO<sub>2</sub>/H<sub>2</sub>O ratio (Pilling et al. 2010). This persistence is attributed to the degradation of complex organic molecules, which are synthesized from simple species during irradiation and subsequently broken down into smaller fragments, including CO and CO<sub>2</sub> (Gerakines et al. 2001). This feedback mechanism creates a dynamic CO-CO<sub>2</sub> equilibrium environment in which CO<sub>2</sub> dominates the volatile inventory, while CO is continuously regenerated from organic decomposition. While laboratory experiments are typically conducted over short timescales and at high irradiation fluxes with relatively simple ice mixtures, making direct extrapolation to gigayear-scale astrophysical environments uncertain, the fundamental radiolysis pathways leading to CO<sub>2</sub> enrichment and CO persistence are robust and well characterized.

Monte Carlo radiation transport simulations with the COMETCOSMIC code, built on GEANT4, show that GCR are the dominant long-term radiation source in cometary nuclei (Gronoff et al. 2020). Energy deposition is controlled mainly by primary protons and their secondary electromagnetic cascades. The deposited dose decreases with depth but remains significant to 15–20 m, with detectable deposition extending to  $\sim 100$  m. Short-lived supernova cosmicray events can increase the dose by orders of magnitude, but only for timescales of  $10^4$ – $10^5$  yr and thus contribute negligibly to the integrated Gyr-scale budget compared to steady GCR irradiation.

Building on the dose deposition results, Maggiolo et al. (2020) show that over 4.5 Gyr of GCR irradiation, the outer 10-20 m of a comet nucleus similar to 67P would undergo chemical and structural changes. To translate the dose deposition into compositional effects, they applied laboratory radiolysis yields from  $H_2O$ –CO mixtures (Hudson & Moore 1999) and pure  $H_2O$  ice (Johnson & Quickenden 1997), predicting the formation of  $O_2$ ,  $H_2O_2$ , and  $CO_2$ , with  $CO_2$  produced effectively in  $H_2O$ –CO ice mixtures. Using the Hudson & Moore (1999) yield, they find that essentially all CO initially present in  $H_2O$ –CO ices can be converted into  $CO_2$  within the first  $\sim 10$  m of the surface after 4.5 Gyr of GCR exposure. In addition to  $CO_2$ , the model predicts the accumulation of  $O_2$  and  $H_2O_2$  in the irradiated layers. Because molecular diffusion is limited at cometary temperatures, these products remain confined to a shallow processed zone. Irradiation also induces amorphization and compaction of ice layers, modifying the physical structure of the crust. Maggiolo et al. (2020) further evidence the production of  $^{15}N$  from GCR-induced spallation of  $^{16}O$ , where neutrons generated by high-energy particle impacts (1 MeV–1 TeV nucleon<sup>-1</sup>) are captured to form heavier nuclei, yielding  $^{15}N$  mainly through the reaction  $n + ^{16}O \rightarrow ^{15}N + d + e^-$ . The production of  $^{15}N$  remains very low, with a maximum increase of the  $^{15}N/^{14}N$  ratio of  $\sim 2 \times 10^{-4}$  after 4.5 Gyr of irradiation by GCR. This is about a factor of 25 too low to explain the high  $^{15}N/^{14}N$  ratio observed in comets (see Gronoff et al. 2020). However, it could be significant for a body with a low initial  $^{15}N/^{14}N$  ratio.

Energetic particle irradiation of icy surfaces, such as those found on comets and trans-Neptunian objects, drives the radiolytic transformation of simple volatiles (e.g.,  $H_2O$ ,  $CH_4$ ,  $NH_3$ , CO) into complex, refractory organic residues. This process begins with molecular dissociation and radical formation, followed by recombination into larger macromolecules, ultimately producing a carbon-rich organic crust (Strazzulla & Palumbo 2001). Repeated irradiation increases the complexity of the crust, resulting in surface darkening and spectral reddening. This arises from the preferential destruction of high-albedo ices and the accumulation of organic molecules, which absorb efficiently in the blue and reflect more in the red to near-infrared wavelengths resulting in strong reddening and darkening of spectral reflectance similar to that seen on Centaurs and trans-Neptunian objects (Brunetto et al. 2006). The reddening effect depends not only on radiation dose but also on irradiation temperature, explaining some of the diversity in TNO colors (Zhang et al. 2025)

Merkulova et al. (2025) suggest that GCR processing of cometary nuclei could trigger explosive outbursts during modest heating events (associated, for instance, with a passing star, galactic tide, or cosmic dust impact). They propose that irradiated ice in cometary nuclei gradually accumulates energetic free radicals (e.g., H, OH). Heating events could trigger rapid recombination, releasing heat, converting amorphous ice to crystalline form, building subsurface pressure,

and eventually producing outbursts. Such outbursts could explain the non-gravitational motion of some long-period comets or interstellar objects.

As comets or interstellar objects approach a star, solar heating alters their nuclei. Thermal-evolution models of repeated perihelion passages indicate that CO is depleted more rapidly than CO<sub>2</sub> or H<sub>2</sub>O, while gas escape leads to the accumulation of refractory surface mantles (Prialnik & Bar-Nun 1988). These mantles reduce outgassing and enhance thermal insulation, thereby steepening temperature gradients between surface and subsurface layers (Guilbert-Lepoutre et al. 2015). Mantle formation is therefore widely invoked in comet evolution models and is consistent with the observed suppression of activity in many nuclei (Bockelée-Morvan & Biver 2017). This framework provides a natural explanation for the observed dichotomy: Jupiter-family comets, which have undergone repeated solar processing, typically display CO/H<sub>2</sub>O ratios below a few percent (Ootsubo et al. 2012), whereas dynamically new Oort-cloud comets can retain CO at levels of several tens of percent, consistent with long-term cryogenic storage prior to their first perihelion passage (McKay et al. 2015). A key limitation, however, is that once mantles become sufficiently thick, they suppress the fluxes of both CO and CO<sub>2</sub>, inconsistent with ATLAS's strong CO<sub>2</sub> production (Guilbert-Lepoutre et al. 2015). Thermal evolution may have contributed to the present properties of ATLAS but cannot alone account for its observed volatile ratios.

Thermal processing prior to 3I/ATLAS entry in the solar system cannot be ruled out from current observations. Assessing its contribution is beyond the scope of this paper, which instead focuses on GCR processing. Indeed, unlike thermal evolution, which requires close stellar passages, either in the system where it formed or during subsequent stellar encounters on its way to the solar system, irradiation by GCR is unavoidable. The only uncertainty is the exposure time, although age estimates for 3I/ATLAS point toward several billion years of irradiation.

### 3.2. GCR Processing Depth

To estimate the penetration depth of GCR in the nucleus of 3I/ATLAS, we consider continuous irradiation over 1 Gyr under a flux representative of the interstellar environment of the Oort Cloud, following the approach of Gronoff et al. (2020). The GCR flux is calculated using the modified Badhwar and O'Neill (1992) H-BON10 model (Mertens et al. 2013), which computes ion fluxes across all species. We consider no modulation of the GCR flux by the heliospheric magnetic field, consistent with the conditions expected in the interstellar medium far from the Sun. The assumption of a constant GCR flux is supported by Smith et al. (2019), who analyzed cosmogenic nuclides (e.g.,  $^{41}$ K,  $^{36}$ Cl, and noble gases) in iron meteorites and demonstrated that the GCR intensity has remained stable within  $\pm 10$ –20% over at least the past 1 Gyr.

We adopt a bulk density of 500 kg m<sup>-3</sup> as representative of cometary nuclei, consistent with spacecraft measurements of comet 67P/Churyumov–Gerasimenko, which yielded  $\sim$ 530 kg m<sup>-3</sup> (Pätzold et al. 2016), and with broader estimates for the comet population derived from remote sensing and modelling (Weissman & Lowry 2008). We assume a nucleus composed of water ice (of isotopic composition  $^{16}$ O and  $^{1}$ H) and SiO<sub>2</sub> with a SiO<sub>2</sub>/H<sub>2</sub>O mass ratio of 4, as in Gronoff et al. (2020).

Figure 1 shows the corresponding energy dose deposited by GCR after 1 Gyr of irradiation. The deposited energy peaks at the surface, reaching  $\sim 5 \times 10^{23}$  eV cm<sup>-3</sup>, and decreases with depth into the nucleus to  $\sim 5 \times 10^{22}$  eV cm<sup>-3</sup> at 10 m and  $\sim 3 \times 10^{19}$  eV cm<sup>-3</sup> at 30 m.

From the energy deposition we evaluate the cumulative effects of GCR exposure on both ice structure and chemical composition after 1 Gyr of irradiation (Figures 2 and 3), following the same approach as in Maggiolo et al. (2020) to simulate the effect of GCR irradiation on the nucleus of comet 67P. While these results are based on models and laboratory data that may not fully capture real cometary conditions, they provide a robust indicator of processing depth. The simulations show that 1 Gyr of GCR irradiation is sufficient to significantly alter the physical state of the ice, converting it into compact amorphous ice, and to produce secondary chemical species (CO<sub>2</sub>, CH<sub>4</sub>, H<sub>2</sub>CO, CH<sub>3</sub>OH, HCO) from a CO–H<sub>2</sub>O ice mixture down to depths of approximately 15–20 m.

### 3.3. Erosion Rate Calculation

A key quantitative test of the GCR processing hypothesis is whether the depth of surface erosion during 3I/ATLAS's Solar system passage is small compared to the expected depth of GCR-induced alteration. To compute the erosion of 3I/ATLAS during its solar system crossing, we model the cumulative erosion depth due to volatile outgassing and dust ejection. The method assumes a time-dependent total mass-loss rate, Q(t), derived from available observations of gas and dust activity.

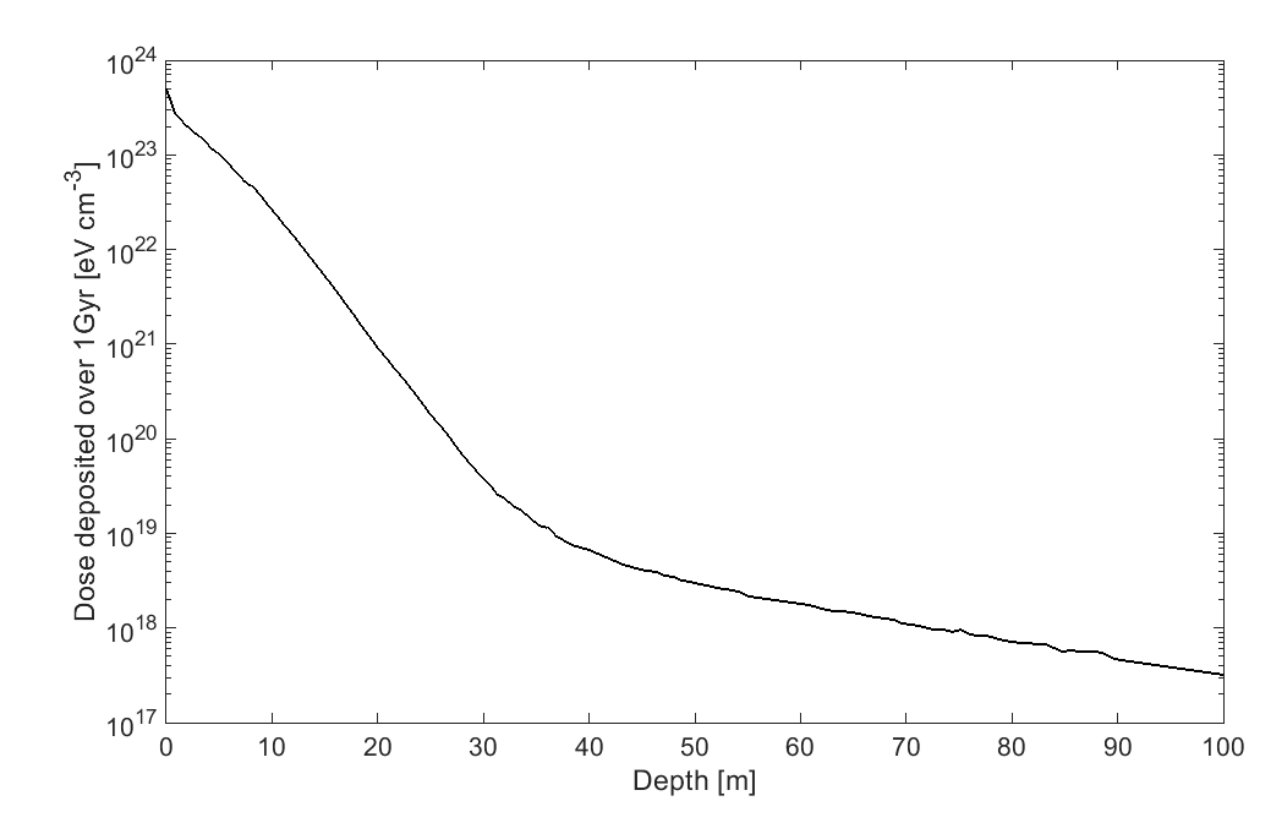


Figure 1. Energy dose deposited by GCRs in a nucleus after an exposure time of 1 Gyr in the local interstellar medium, adapted from Gronoff et al. (2020). The simulation assumes a bulk density of  $0.5~{\rm g\,cm^{-3}}$  and a nucleus composed of  ${\rm H_2O}$  (of isotopic composition  $^{16}{\rm O}$  and  $^{1}{\rm H}$ ) and  ${\rm SiO_2}$  with a  ${\rm SiO_2}/{\rm H_2O}$  mass ratio of 4.

Cometary production rates are typically described by power-law dependencies on heliocentric distance, with the slope  $(\alpha)$  reflecting the dominant sublimating species. For H<sub>2</sub>O-driven activity,  $\alpha$  values near -2 are common under equilibrium conditions (e.g., Krishna Swamy 1991), with steeper slopes up to -4 observed near perihelion, as in 67P/Churyumov–Gerasimenko (Skorov et al. 2020). However, at heliocentric distances beyond  $\sim 3$  au, where water sublimation is inefficient, the activity is more likely driven by hypervolatiles such as CO and CO<sub>2</sub>, for which survey-based fits suggest shallower exponents:  $\alpha \approx -1$  to -2 for CO (Womack et al. 2017) and  $\alpha \approx -2$  to -3 for CO<sub>2</sub> (Ootsubo et al. 2012), while H<sub>2</sub>O-driven activity typically follows  $\alpha \approx -3$  to -5 within  $\sim 3$  au (Combi et al. 2019). Therefore, the commonly cited  $\alpha = -2$  and  $\alpha = -4$  slopes span the expected range for different volatiles, though care must be taken when interpreting them in the context of species-specific drivers. For 3I/ATLAS, we adopt whole-coma production rates from Cordiner et al. (2025),  $Q(\text{CO}_2) = (1.76 \pm 0.02) \times 10^{27} \text{ s}^{-1}$ ,  $Q(\text{CO}) = (3.0 \pm 0.2) \times 10^{26} \text{ s}^{-1}$ ,  $Q(\text{H}_2\text{O}) = (2.19 \pm 0.08) \times 10^{26} \text{ s}^{-1}$ , and  $Q(\text{OCS}) = (4.3 \pm 0.9) \times 10^{24} \text{ s}^{-1}$ . These volatiles collectively correspond to a total gas mass-loss rate of  $\sim 150$  kg s<sup>-1</sup> at 3.32 au. Dust mass-loss estimates are taken from Jewitt et al. (2025), who reported 12–120 kg s<sup>-1</sup> at 3.83 au. We therefore consider two bounding cases: a "minimum" total mass-loss scenario including 12 kg s<sup>-1</sup> of dust, and a "maximum" scenario including 120 kg s<sup>-1</sup> of dust. To capture the uncertainty in heliocentric scaling, we evaluate both  $Q \propto r_{\rm h}^{-2}$  and  $Q \propto r_{\rm h}^{-4}$  dependencies, representing relatively shallow and steep activity laws, respectively.

To translate the mass-loss rate into physical erosion of the nucleus, we consider two possible nucleus radii for 3I/ATLAS, following the size estimates reported by Jewitt et al. (2025): 500 m and 2200 m. These values bracket the plausible size range and allow us to assess how erosion depth scales with nucleus size. We use a bulk density of 500 kg m<sup>-3</sup>, consistent with the value adopted in Section 3.2.

The erosion depth as a function of time is shown in Figure 4. The heliocentric distance of 3I/ATLAS is derived from its current orbital parameters. The results indicate that material loss due to sublimation and dust ejection remains limited before perihelion (q = 1.356 au on 2025-10-29 11:44 UT), with the bulk of the erosion occurring in the vicinity

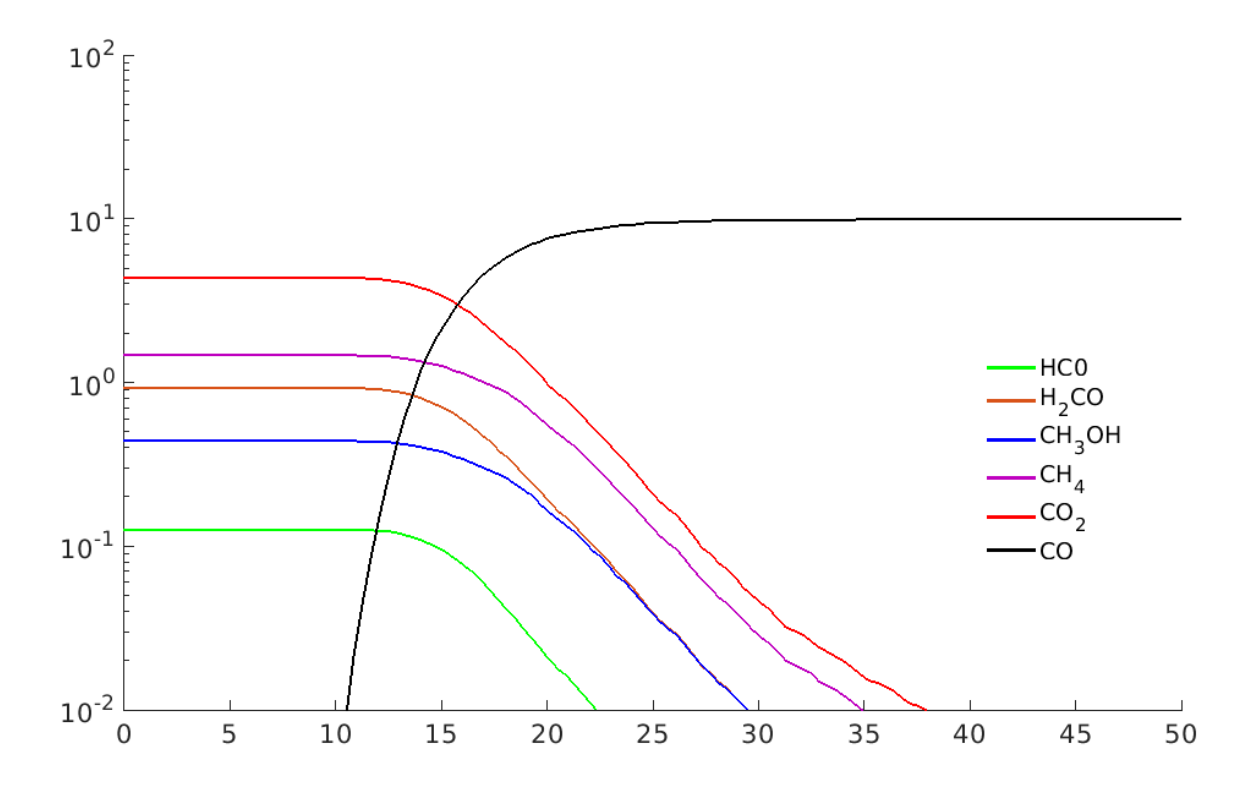


Figure 2. Depth profiles of chemical abundances relative to  $H_2O$  in a nucleus irradiated by galactic cosmic rays, adapted from Maggiolo et al. (2020). The simulation assumes a bulk density of 0.5 g cm<sup>-3</sup>, an exposure time of 1 Gyr, and mixed  $H_2O$ -CO ices. Radiolysis yields are taken from laboratory experiments by Hudson & Moore (1999), while the depth-dependent energy deposition is based on Monte Carlo radiation transport results from Gronoff et al. (2020). CO (black) is progressively converted into  $CO_2$  (red) within the outer  $\sim$ 15–20 m, while other products (CH<sub>4</sub>, CH<sub>3</sub>OH, H<sub>2</sub>CO, HCO) decrease with depth as irradiation effects diminish.

of perihelion, where solar insolation, and hence mass loss, is the highest. Pre-perihelion erosion remains shallow, below  $\sim 1$  m. Near perihelion, the erosion rate rises sharply, leading to total erosion depths of several tens of meters in strong outgassing scenarios. In contrast, for low and moderate outgassing scenarios, post-perihelion erosion remains well below the thickness of the GCR-processed crust (15–20 m).

## 3.4. Implications for Outgassing Material

Prior to perihelion, the cumulative erosion depth of 3I/ATLAS remains well below the  $\sim 15-20$  m depth to which GCR are expected to chemically and structurally modify cometary material over  $\sim 1$  Gyr of exposure (see Figures 2 and 3). This indicates that the volatiles released during the inbound leg of the orbit originate predominantly from GCR-processed surface layers. Post-perihelion, this conclusion remains valid for larger nucleus sizes, independent of the assumed heliocentric dependence of the activity. However, for small-nucleus scenarios (radii of a few hundred meters) combined with steep heliocentric activity laws (e.g.,  $Q \propto r_{\rm h}^{-4}$ ), the erosion depth can exceed the cosmic-ray penetration threshold. In such cases, post-perihelion outgassing may begin to expose and release unprocessed, pristine material from the interior.

A close passage near a star, either the parent star prior to ejection or another star encountered during interstellar transit, represents a potential scenario that could result in 3I/ATLAS outgassing pristine material. In this case, thermal processing induced by stellar radiation could have sublimated and removed pre-existing irradiated surface layers formed by long-term GCR exposure, thereby exposing deeper, unaltered ices. A collision could also redistribute the irradiated material (see the discussion in Maggiolo et al. 2020). If the collision is catastrophic, the nucleus material is altered, and the material within a body that would form from the reaggregation of the fragments could not be considered pristine anymore. In the case of a sub-catastrophic or marginally catastrophic collision, the nucleus material (both

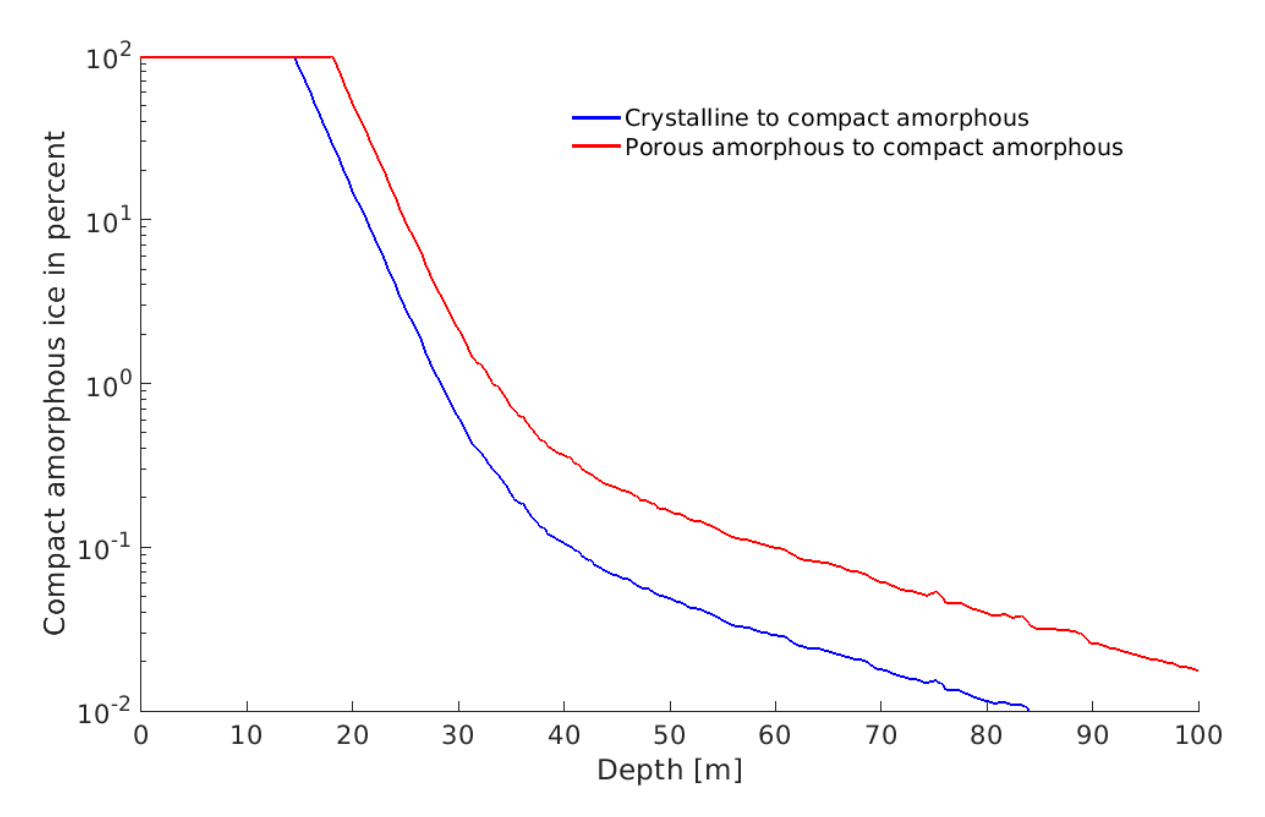


Figure 3. Depth-dependent transformation of ice structure under galactic cosmic rays irradiation, adapted from Maggiolo et al. (2020). The simulation assumes a bulk density of  $0.5 \text{ g cm}^{-3}$  and an exposure time of 1 Gyr, with energy deposition rates from Gronoff et al. (2020). Transformation yields from Dartois et al. (2013) for porous amorphous ice and Dartois et al. (2015) for crystalline ice are applied to compute the compact amorphous fraction (in %), showing the progressive conversion of crystalline  $H_2O$  ice (blue) and porous amorphous ice (red). The conversion is most efficient within the outer tens of meters and decreases with depth.

processed by GCR and not processed by GCR) is mostly unaltered. The fragments resulting from such a collision could reaggregate to form a new nucleus and irradiated material may end up deep inside the newly formed nucleus. If collision debris are large enough and diffusion in the reformed nucleus limited, this could be a source of nucleus inhomogeneity.

However, both the stellar-encounter and collision scenarios would lead to the release of pristine material only if they occurred recently enough to prevent the reformation of a thick irradiated crust. Just below the surface, where GCR energy deposition is highest, the timescale to deplete CO is on the order of 500 Myr (Maggiolo et al. 2020). The conversion of low-temperature porous amorphous ice or of crystalline ice into compact amorphous ice is quite efficient (Dartois et al. 2013, 2015). In the near-surface region where GCR energy deposition peaks, structural modifications of the ice occur on relatively short timescales. At a depth of  $\sim$ 2 m, the transition from crystalline to amorphous ice proceeds over  $\sim$ 60 Myr, while amorphous ice compacts over  $\sim$ 15 Myr (Maggiolo et al. 2020). As shown in Figures 2 and 3, 1 Gyr of GCR irradiation is sufficient to produce a chemically and structurally altered layer tens of meters thick.

In addition to chemical processing, physical erosion due to cosmic-ray-induced sputtering has also been considered. However, laboratory-based sputtering yields indicate that, for a typical interstellar GCR ionization rate of  $\sim 10^{-16} \ \rm s^{-1}$ , sputtering fluxes range from  $\sim 1$  to  $10^3$  molecules cm<sup>-2</sup> s<sup>-1</sup> for common ices such as H<sub>2</sub>O, CO<sub>2</sub>, and CO (Dartois et al. 2023). Integrated over 1 Gyr, this corresponds to the loss of  $\sim 3.2 \times 10^{16}$  to  $3.2 \times 10^{19}$  molecules cm<sup>-2</sup>, equivalent to erosion of only  $\sim 0.3~\mu \rm m$  to  $0.3~\mu \rm m$  of surface material (assuming  $\sim 10^{22}$  molecules cm<sup>-3</sup>). This confirms earlier conclusions that GCR-induced sputtering does not significantly contribute to surface removal over Gyr timescales and therefore cannot account for the exposure of unirradiated subsurface layers.

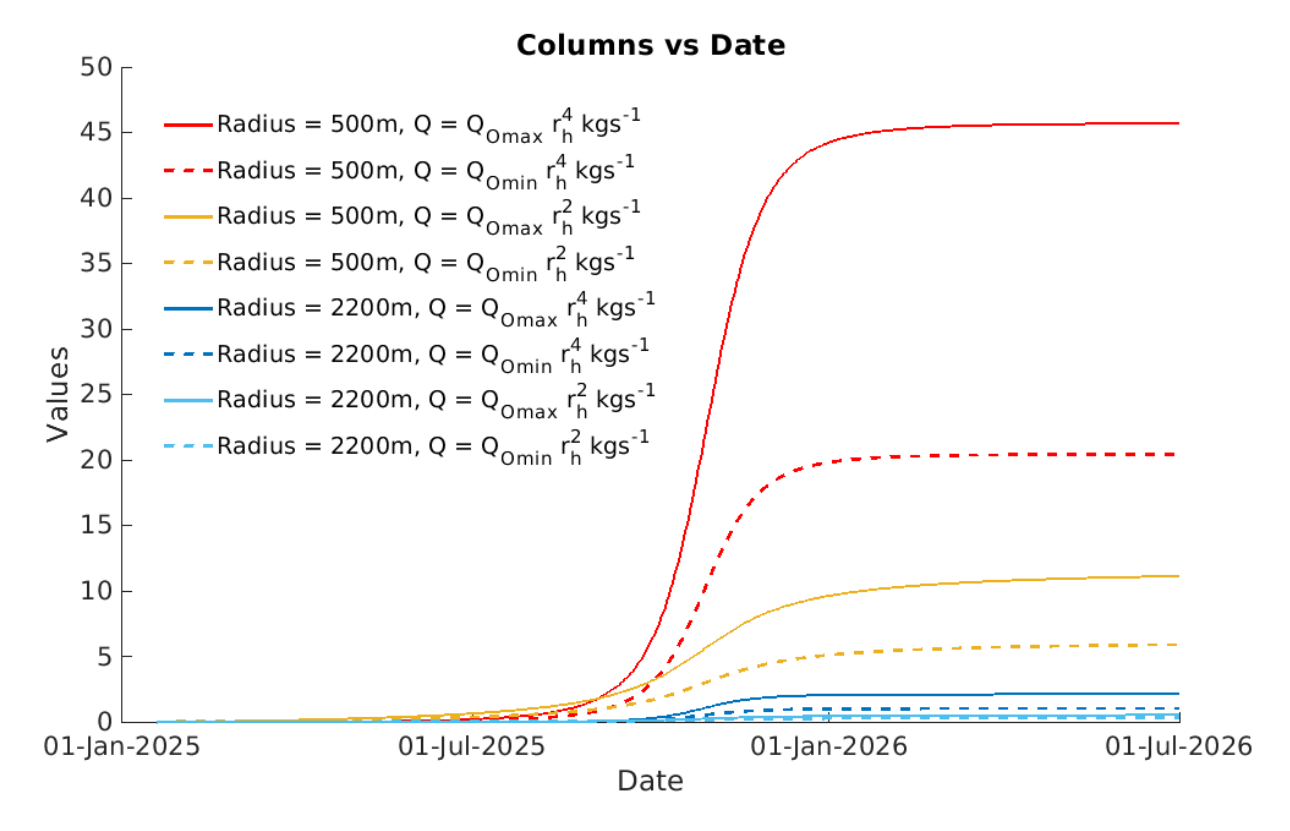


Figure 4. Cumulative erosion depth of 3I/ATLAS as a function of time during its solar system passage, scaled with heliocentric distance from the object's orbital parameters. Mass-loss rates are modeled as power laws in heliocentric distance ( $Q \propto r_{\rm h}^{-2}$  and  $Q \propto r_{\rm h}^{-4}$ ) and anchored to gas production from Cordiner et al. (2025) and dust production from Jewitt et al. (2025). Solid curves represent maximum dust-loss scenarios (120 kg s<sup>-1</sup> at 3.83 AU), while dashed curves represent minimum dust-loss scenarios (12 kg s<sup>-1</sup> at 3.83 AU). Two nucleus radii are considered: 500 m and 2200 m.

Taken together, these considerations support the conclusion that the volatiles observed in 3I/ATLAS prior to perihelion are consistent with release from GCR-processed material, unless a recent resurfacing event, such as a close stellar encounter or collision, removed or redistributed the irradiated mantle and exposed deeper, pristine ices.

#### 4. IMPLICATIONS AND PARADIGM SHIFT

Rather than being pristine messengers from distant planetary systems, interstellar objects may instead carry signatures of processed material shaped by Gyr-scale cosmic-ray exposure both in the distant reservoirs of their parent stellar systems, prior to ejection, and during their interstellar transit to the solar system.

## 4.1. 3I/ATLAS: From Pristine to Processed

It is often assumed that interstellar objects retain the primordial compositions acquired in their formation environments (Jewitt & Seligman 2023).

However, beyond any storage within their parent stellar systems, interstellar objects can reside in the dalactic environment for *Gyr-scale* times, as inferred for the first two interlopers and particularly for 3I/ATLAS (Jewitt & Seligman 2023; Taylor & Seligman 2025). Their surface layers have been exposed to cosmic-ray irradiation for sufficiently long periods to drive extensive alteration of their outer layers. The processed zone, estimated to extend 15–20 m deep, surpasses pre-perihelion erosion depths, implying that pre-perihelion observations generally probe altered rather than pristine material. Because most erosion occurs near perihelion, some of these objects may only expose unprocessed interior material after perihelion, depending on their orbital dynamics, outgassing rates, and sizes.

This reinterpretation fundamentally alters how we interpret spectroscopic measurements of 3I/ATLAS. Rather than sampling primordial material that reveals distant formation conditions, we are observing the products of Gyr-scale galactic cosmic-ray chemistry. The extreme  $\rm CO_2/H_2O$  ratio reflects processing efficiency, not formation environment.

The substantial CO levels indicate ongoing chemical evolution, not pristine composition. This study suggests that 3I/ATLAS is better understood as a natural laboratory for cosmic-ray processing than as a direct messenger from a distant protoplanetary disk. This concept is summarized in Figure 5, which illustrates the stratigraphy of an irradiated nucleus, with a GCR-processed crust overlying a pristine interior shielded from cosmic rays.

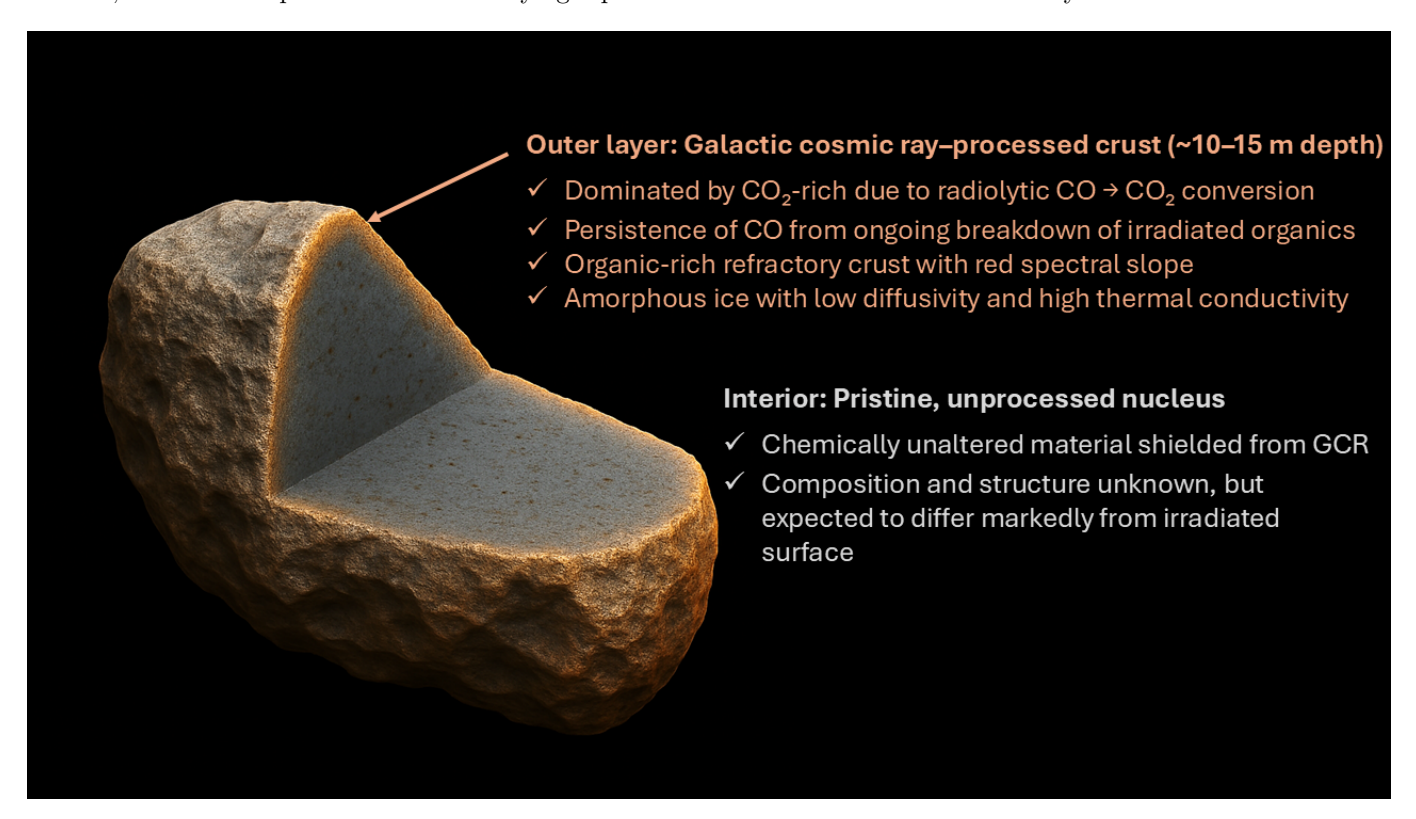


Figure 5. Schematic illustration of interstellar comet 3I/ATLAS showing the expected stratigraphy of an irradiated nucleus. Galactic cosmic ray irradiation over several Gyr alters the outer  $\sim 15-20$  m, producing a  $CO_2$ -rich crust through CO-to- $CO_2$  conversion, ongoing CO release from the breakdown of irradiated organics, an organic-rich refractory mantle with a red spectral slope, and compact amorphous ice characterized by low diffusivity and high thermal conductivity. Beneath this layer lies a pristine, unprocessed interior shielded from GCRs, whose composition and structure remain unknown but are expected to differ markedly from the irradiated crust.

## 4.2. Future Observational Strategy for Interstellar Objects

This paradigm shift defines clear observational priorities. For 3I/ATLAS, key tests include JWST/MIRI searches for organic features diagnostic of irradiation processing, thermal mapping to distinguish altered surface layers from low-conductivity insulating mantles, and continued monitoring of volatile ratios, in particular for the main products of  $H_2O$  and  $CO_2$  ice radiolysis such as  $CO_2$ ,  $O_2$ ,  $H_2$ , and  $H_2O_2$ . Comparing pre- and post-perihelion activity is especially valuable, since post-perihelion outgassing may probe deeper layers less affected by GCR irradiation.

Looking ahead, the Vera C. Rubin Observatory could detect up to 70 interstellar objects annually (Marčeta & Seligman 2023), enabling statistical tests of how widespread cosmic-ray processing is among such bodies. Rather than attributing compositional diversity solely to differences in formation environments, population studies must account for systematic ageing effects linked to interstellar residence times.

### 5. CONCLUSION

Multi-instrument observations of interstellar comet 3I/ATLAS reveal an unprecedented  ${\rm CO_2/H_2O}$  ratio of  $7.6\pm0.3$  (Cordiner et al. 2025), the most extreme volatile composition ever recorded in a comet. This value lies  $4.5\,\sigma$  above solar system trends and exceeds the typical cometary median of 0.12 reported by Harrington-Pinto et al. (2022) for 25 solar system comets by a factor of  $\sim6763$ , requiring explanation through evolutionary processing rather than primordial inheritance.

The combined evidence, including extreme  $CO_2$  enrichment, sustained CO and  $H_2O$  outgassing, and red spectral slopes (16–27% per kÅ), points toward Gyr-scale galactic cosmic ray processing as the dominant mechanism shaping 3I/ATLAS's current properties. Laboratory irradiation experiments demonstrate that GCRs efficiently convert CO into  $CO_2$  while producing organics and compact amorphous ice (Hudson & Moore 1999; Palumbo 1997). Radiation transport models show that such processing alters the nucleus down to depths of 15–20 m (Gronoff et al. 2020; Maggiolo et al. 2020). Estimations of 3I/ATLAS erosion confirm that present-day activity exposes only this GCR-processed crust, while the pristine interior remains shielded.

This reinterpretation represents a paradigm shift: interstellar objects cannot be assumed to be pristine messengers of their formation environments. Instead, they serve as natural laboratories of long-term cosmic-ray chemistry.

With perihelion in October 2025, time-sensitive observations remain crucial. JWST/MIRI searches for organic features, thermal mapping of insulating crusts, and continued volatile monitoring can critically constrain the extent of GCR-induced alteration.

#### ACKNOWLEDGMENTS

JDK and FD are supported by ESA/PRODEX Comet Interceptor under contract PEA 4000139830

#### AUTHOR CONTRIBUTIONS

R. M. came up with the initial research concept, participated to the development and design of methodology; participated to the creation of models; edited the manuscript and was responsible for writing and submitting the manuscript. F. D. participated to the preparation, creation and presentation of the published work, specifically writing the initial draft. G. G. came up with the initial research concept; participated to the development and design of methodology and participated to the creation of models. J. de K. and G. C. participated to the preparation, creation and presentation of the published work.

## REFERENCES

- Baratta, G. A., Leto, G., & Palumbo, M. E. 2002, A&A, 384, 343, doi: 10.1051/0004-6361:20011835
- Belyakov, M., Fremling, C., Graham, M. J., et al. 2025, Research Notes of the AAS, 9, 194, doi: 10.3847/2515-5172/adf059
- Beniyama, J. 2025, Publications of the Astronomical Society of Japan, psaf097, doi: 10.1093/pasj/psaf097
- Bockelée-Morvan, D., & Biver, N. 2017, Phil. Trans. R. Soc. A, 375, 20160252, doi: 10.1098/rsta.2016.0252
- Bodewits, D., Noonan, J. W., Feldman, P. D., et al. 2020, Nat. Astron., 4, 867, doi: 10.1038/s41550-020-1095-2
- Bolin, B. T., Belyakov, M., Fremling, C., et al. 2025, MNRAS, 542, L139, doi: 10.1093/mnrasl/slaf078
- Boogert, A. C. A., Gerakines, P. A., & Whittet, D. C. B. 2015, ARA&A, 53, 541,
  - doi: 10.1146/annurev-astro-082214-122348
- Bosman, A. D., Walsh, C., & van Dishoeck, E. F. 2018, A&A, 615, doi: 10.1051/0004-6361/201833497
- Brunetto, R., Barucci, M. A., Dotto, E., & Strazzulla, G. 2006, ApJ, 644, 646, doi: 10.1086/503359

- Combi, M. R., Mäkinen, T. T., Bertaux, J.-L., Quémerais, E., & Ferron, S. 2019, Icarus, 317, 610, doi: 10.1016/j.icarus.2018.08.031
- Cordiner, M. A., Milam, S. N., Biver, N., et al. 2020, Nat. Astron., 4, 861, doi: 10.1038/s41550-020-1087-2
- Cordiner, M. A., Roth, N. X., Kelley, M. S. P., et al. 2025,
   The Astrophysical Journal Letters, 991, L43,
   doi: 10.3847/2041-8213/ae0647
- Dartois, E., Chabot, M., Da Costa, C. A. P., et al. 2023, A&A, 671, doi: 10.1051/0004-6361/202245383
- Dartois, E., Ding, J. J., de Barros, A. L. F., et al. 2013, A&A, 557, doi: 10.1051/0004-6361/201321636
- Dartois, E., Augé, B., Boduch, P., et al. 2015, A&A, 576, doi: 10.1051/0004-6361/201425415
- Denneau, L., Siverd, R., Tonry, J., et al. 2025, Minor Planet Electronic Circulars, 2025-N12, doi: 10.48377/MPEC/2025-N12
- de León, J., Licandro, J., de la Fuente Marcos, C., et al. 2020, Monthly Notices of the Royal Astronomical Society, 495, 2053, doi: 10.1093/mnras/staa1190
- Drozdovskaya, M. N., Walsh, C., van Dishoeck, E. F., et al. 2016, MNRAS, 462, 977, doi: 10.1093/mnras/stw1632

- Eistrup, C., Walsh, C., & van Dishoeck, E. F. 2018, A&A, 613, doi: 10.1051/0004-6361/201731302
- —. 2019, A&A, 629, A84, doi: 10.1051/0004-6361/201935812
- Fitzsimmons, A., Dahlgren, M., Lagerkvist, C. I., Magnusson, P., & Williams, I. P. 1994, A&A, 282, 634
- Fitzsimmons, A., Snodgrass, C., Rozitis, B., et al. 2018, Nat. Astron., 2, 133, doi: 10.1038/s41550-017-0361-4
- Fornasier, S., Barucci, M. A., de Bergh, C., et al. 2009, A&A, 508, 457, doi: 10.1051/0004-6361/200912582
- Fraser, W. C., & Brown, M. E. 2012, ApJ, 749, 33, doi: 10.1088/0004-637X/749/1/33
- Gerakines, P. A., Moore, M. H., & Hudson, R. L. 2001, Journal of Geophysical Research: Planets, 106, 33381, doi: 10.1029/2000JE001320
- Gronoff, G., Maggiolo, R., Cessateur, G., et al. 2020, The Astrophysical Journal, 890, 89, doi: 10.3847/1538-4357/ab67b9
- Guilbert-Lepoutre, A., Besse, S., Mousis, O., et al. 2015, SSRv, 197, 271, doi: 10.1007/s11214-015-0148-9
- Harrington-Pinto, O., Womack, M., & Fernandez, Y. R. 2022, PSJ, 3, 247, doi: 10.3847/PSJ/ac960d
- Hopkins, M. J., Dorsey, R. C., Forbes, J. C., et al. 2025,The Astrophysical Journal Letters, 990, L30,doi: 10.3847/2041-8213/adfbf4
- Hudson, R. L., & Moore, M. H. 1999, Icarus, 140, 451, doi: 10.1006/icar.1999.6144
- Jewitt, D., Hui, M. T., Mutchler, M., Kim, Y., & Agarwal, J. 2025, ApJL, 990, doi: 10.3847/2041-8213/adf8d8
- Jewitt, D., & Seligman, D. Z. 2023, ARA&A, 61, 197, doi: 10.1146/annurev-astro-071221-054221
- Johnson, R. E., & Quickenden, T. I. 1997, Journal of Geophysical Research: Planets, 102, 10985, doi: 10.1029/97JE00068
- Kareta, T., Champagne, C., McClure, L., et al. 2025, ApJL, 990, doi: 10.3847/2041-8213/adfbdf
- Krishna Swamy, K. S. 1991, A&A, 241, 260
- Lisse, C. M., Bach, Y. P., Bryan, S., et al. 2025, Research Notes of the AAS, 9, 242, doi: 10.3847/2515-5172/ae0293
- Maggiolo, R., Gronoff, G., Cessateur, G., et al. 2020, ApJ, 901, 136, doi: 10.3847/1538-4357/abacc3
- Marčeta, D., & Seligman, D. Z. 2023, PSJ. https://arxiv.org/abs/2310.17575
- Marcos de la Fuente, R., Alarcón, M. R., Licandro, J., et al. 2025, A&A, 700, doi: 10.1051/0004-6361/202556439
- McClure, M. K., Rocha, W. R. M., Pontoppidan, K. M., et al. 2023, Nat. Astron., 7, 431, doi: 10.1038/s41550-022-01875-w
- McKay, A. J., Cochran, A. L., DiSanti, M. A., et al. 2015, Icarus, 250, 504, doi: 10.1016/j.icarus.2014.12.023

- Mennella, V., Palumbo, M. E., & Baratta, G. A. 2004, ApJ, 615, 1073, doi: 10.1086/424685
- Merkulova, A. Y., Pavlov, A. K., & Belousov, D. V. 2025, Icarus, 434, 116547, doi: 10.1016/j.icarus.2025.116547
- Mertens, C. J., Meier, M. M., Brown, S., Norman, R. B., & Xu, X. 2013, Space Weather, 11, 603, doi: 10.1002/swe.20100
- Micheli, M., Farnocchia, D., Meech, K. J., et al. 2018, Nature, 559, 223, doi: 10.1038/s41586-018-0254-4
- Mousis, O., Lunine, J. I., Picaud, S., & Cordier, D. 2010, Faraday Discuss., 147, 509, doi: 10.1039/c003658g
- Ootsubo, T., Kawakita, H., Hamada, S., et al. 2012, ApJ, 752, 15, doi: 10.1088/0004-637X/752/1/15
- Opitom, C., et al. 2025, MNRAS, 544, L31, doi: 10.1093/mnrasl/slaf095
- Palumbo, M. E. 1997, Advances in Space Research, 20, 1637, doi: 10.1016/S0273-1177(97)00823-5
- Pätzold, M., Andert, T., Hahn, M., et al. 2016, Nature, 530, 63, doi: 10.1038/nature16535
- Pilling, S., Seperuelo Duarte, E., Domaracka, A., et al. 2010, A&A, 523, doi: 10.1051/0004-6361/201015123
- Prialnik, D., & Bar-Nun, A. 1988, Icarus, 74, 272, doi: 10.1016/0019-1035(88)90042-5
- Price, E. M., Cleeves, L. I., Bodewits, D., & Öberg, K. I. 2021, ApJ, 913, 9, doi: 10.3847/1538-4357/abf041
- Satorre, M., Palumbo, M., & Strazzulla, G. 2000,
   Astrophysics and Space Science, 274, 643,
   doi: 10.1023/A:1026512023613
- Seccull, T., Fraser, W. C., & Puzia, T. H. 2021, PSJ, 2, 239, doi: 10.3847/PSJ/ac33b1
- Seligman, D. Z., & Laughlin, G. 2020, ApJL, 896, doi: 10.3847/2041-8213/ab963f
- Seligman, D. Z., Micheli, M., Farnocchia, D., et al. 2025, The Astrophysical Journal Letters, 989, L36, doi: 10.3847/2041-8213/adf49a
- Semenov, D., Wiebe, D., & Henning, T. 2004, A&A, 417, 93, doi: 10.1051/0004-6361:20034128
- Skorov, Y., Keller, H. U., Mottola, S., & Hartogh, P. 2020, MNRAS, 494, 3310, doi: 10.1093/mnras/staa865
- Smith, T., Cook, D. L., Merchel, S., et al. 2019, Meteorit. Planet. Sci., 54, 2951, doi: 10.1111/maps.13417
- Souza-Feliciano, A. C., Holler, B. J., Pinilla-Alonso, N., et al. 2024, A&A, 681, L17, doi: 10.1051/0004-6361/202348222
- Strazzulla, G., & Palumbo, M. 2001, Advances in Space Research, 27, 237,
  - doi: https://doi.org/10.1016/S0273-1177(01)00053-9
- Taylor, A. G., & Seligman, D. Z. 2025, The Astrophysical Journal Letters, 990, L14, doi: 10.3847/2041-8213/adfa28

- Tonry, J. L., Denneau, L., Heinze, A. N., et al. 2018, PASP, 130, 064505, doi: 10.1088/1538-3873/aabadf
- Weissman, P. R., & Lowry, S. C. 2008, Meteoritics & Planetary Science, 43, 1033,

doi: https://doi.org/10.1111/j.1945-5100.2008.tb00691.x

- Womack, M., Sarid, G., & Wierzchos, K. 2017, PASP, 129, 031001, doi: 10.1088/1538-3873/129/973/031001
- Xing, Z., Oset, S., Noonan, J., & Bodewits, D. 2025, The Astrophysical Journal Letters, 991, L50, doi: 10.3847/2041-8213/ae08ab
- Zhang, C., Wang, J., Turner, A. M., Young, L. A., & Kaiser, R. I. 2025, The Astrophysical Journal Supplement Series, 278, 30, doi: 10.3847/1538-4365/adc718